ACS APPLIED MATERIALS & INTERFACES

Research Article

www.acsami.org

WO_{3-x} Nanoplates Grown on Carbon Nanofibers for an Efficient Electrocatalytic Hydrogen Evolution Reaction

JiaDong Chen, DanNi Yu, WeiSha Liao, MengDan Zheng, LongFei Xiao, Han Zhu, Ming Zhang, MingLiang Du,* and JuMing Yao

Key Laboratory of Advanced Textile Materials and Manufacturing Technology of the Ministry of Education, College of Materials and Textiles, Zhejiang Sci-Tech University, Hangzhou 310018, P. R. China

Supporting Information

ABSTRACT: The search for non-noble metal catalysts with high activity for the hydrogen evolution reaction (HER) is crucial for efficient hydrogen production at low cost and on a large scale. Herein, we report a novel WO_{3-x} catalyst synthesized on carbon nanofiber mats (CFMs) by electrospinning and followed by a carbonization process in a tubal furnace. The morphology and composition of the catalysts were tailored via a simple method, and the hybrid catalyst mats were used directly as cathodes to investigate their HER performance. Notably, the as-prepared catalysts exhibit substantially enhanced activity for the HER, demonstrating a small overpotential, a high exchange current density, and a large cathodic current density. The remarkable electrocatalytic performances result from the poor crystallinity of WO_{3-x}, the high electrical conductivity of WO_{3-x}, and the use of electrospun CNFs. The present work outlines a straightforward approach for the synthesis of transition metal oxide (TMO)-based carbon nanofiber mats with promising applications for the HER.

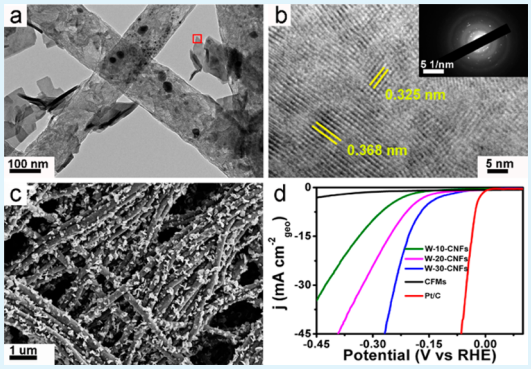

KEYWORDS: *two-dimension, carbon nanofibers, electrocatalysis, hydrogen evolution, WO_{3-x}*

1. INTRODUCTION

As a green fuel of the future, hydrogen has the potential to become an exceptional substitute for traditional fossil fuels. As is well-known, water electrolysis is an essential strategy to generate hydrogen.[1] To accomplish the efficient electrochemical splitting of water for various applications, active electrochemical catalysts for the hydrogen evolution reaction (HER) are crucial.[2] To date, various catalysts have been explored for such applications.[3] Although some precious metals (e.g., platinum) have been shown to be efficient for the HER, their scarcity and high cost impede their practical applications on a large scale.[4] Therefore, developing nonprecious metal catalysts has been widely investigated. Metal oxides,[5,6] metal sulfides,[7,8] metal borides,[9,10] metal phosphides,[11] metal carbides,[12,13] and metal selenides[14] are typical candidates for water splitting. Currently, because of their abundance, stability, and accessibility, transition metal oxides (TMOs), including tungsten oxides,[6] molybdenum oxides,[5] and cobalt oxides,[15] have attracted considerable attention. Notably, it has been reported that oxygen vacancies in TMOs are critical for the efficient production of hydrogen.[6] These vacancies provide active sites for the catalysts, which increase its conductivity and raise its electrocatalytic performance.[16] Hence, TMOs with a large number of oxygen vacancies are excellent candidates for use in the HER because of their active and metallic nature. Among the various TMO catalysts for the HER, transition metal (e.g., Mo and W) oxides have recently been given added attention. For example, Wu et al. prepared metallic WO_2-carbon mesoporous nanowires (MWCMNs) by calcination of WO_3-ethylenediamine hybrid precursors.[6] The products showed superior electrocatalytic activity and stability compared to the WO_3 porous nanowires. The enhancement of the HER performance was primarily attributed to the presence of a large number of oxygen vacancies, which have been shown to act as active sites for the HER.[6] In addition, Jin and Shen reported nanoflower-like metallic MoO_2 electrocatalysts on nickel foam (NF).[5] In this case, the NF-supported MoO_2 also exhibited excellent performance for hydrogen generation; indeed, the onset overpotential was reported to be only 10 mV.[5] Therefore, transition metal (e.g., Mo and W) oxides are promising candidates as electrocatalysts for the HER.

Because of the strong metal−metal bonding in the crystal structures of tungsten suboxides and dioxides and the various oxygen vacancy defects in their lattices, WO_2 and WO_{3-x} possess metallic conductivity (e.g., the conductivity of WO_2 is ~350 S cm^{-1})[17,18] and are thus expected to have high potential activity. However, until now, it has been challenging to synthesize these metallic TMOs supported on highly conductive substrates with nanostructures containing a high number of active sites and a larger specific area because of the

Received: May 2, 2016
Accepted: June 29, 2016

DOI: 10.1021/acsami.6b05245
ACS Appl. Mater. Interfaces XXXX, XXX, XXX−XXX

complicated synthetic process and/or the instability of the products.[14,19] Polymer binders such as Nafion are widely employed to immobilize electrocatalysts on the electrodes for applications or measurements.[20] However, polymer binders may reduce the catalytic efficiency of the electrochemical catalysts because they reduce the permeability of gas and block the active sites. Therefore, avoiding the use of polymer binders in the preparation of electrocatalysts is preferred. Moreover, because of their high conductivity and large specific area, electrospun carbon nanofiber mats synthesized from polyacrylonitrile (PAN) nanofibers have been widely employed as substrates for HER catalysts.[21]

According to the carbothermal reduction theory of WO_3, the formation of tungsten carbides follows the sequence $WO_3 \rightarrow WO_{3-x} \rightarrow W \rightarrow W_2C$.[22] Generally, a high carbon excess condition is required to generate both W and W_2C.[22,23] The formation of WO_{3-x} is more favorable at lower carbon excess conditions than the formation of W and W_2C.[24,25] Therefore, the desired material can be crafted in a favorable manner by changing the amount of thermally active carbon around WO_3 during the fabrication process. With relatively less active carbon, WO_3 is prone to partially reduce to give WO_{3-x}.[26,27] In fact, reducing the amount of thermally active carbon or increasing the amount of WO_3 are both viable approaches to generate WO_{3-x}. Previously, Zou et al. synthesized poor crystallized $W(Se_xS_{1-x})_2$ nanoflakes via incorporating Se element to WS_2 nanoflakes. The defects in the crystal structure served as active sites and dramatically improved the electrocatalytic HER performance.[28] As discussed above, typically oxygen vacancies are active sites of tungsten oxides for HER.[6] Subsequently, in the present investigations, we proposed a facile method to fabricate oxygen vacancy-abundant WO_{3-x} catalysts in carbon nanofibers (CNFs) via carbon thermal reduction reaction at high temperature. The as-prepared products were obtained by thermally annealing tungsten–polyacrylonitrile (W-PAN) precursors in air and argon gas. By tuning the tungsten chloride content in the W-PAN precursor, we obtained the component transition from W_2C to WO_{3-x} on the CNFs. The synthesized catalysts were then used directly as binder-free electrodes.

2. EXPERIMENTAL SECTION

2.1. Preparation of PAN nanofiber mats and tungsten chloride hydrate containing PAN FMs. Polyacrylonitrile nanofiber mats (PAN FMs) were prepared via an electrospinning technique. PAN powder (1.28 g) was dissolved in 10 mL of dimethylformamide (DMF, 99.5%, from Aldrich) under magnetic stirring until a homogeneous solution was obtained. The mass ratio of PAN in the DMF solution was 12%. The solution was transferred to a syringe with a stainless copper needle at the tip. The needle was connected to a high voltage power supply. The fixed voltage was set to 12 kV, and the needle-to-collector distance was 12 cm. The flow rate was set to 0.01 mL min^{-1}. The electrospinning procedure was performed at room temperature. The electrospun nanofiber mats were collected on a piece of aluminum foil. The W-PAN FMs were synthesized by adding additional tungsten chloride powder (WCl_6, 99.80%, from Aldrich) to the as-mentioned PAN/DMF solution by electrospinning under the same conditions. The concentration of WCl_6 is based on the weight of the PAN powder.

2.2. Fabrication of carbon nanofibers, preoxidized W-PAN, and W-CNF nanofiber mats. The as-collected electrospun PAN FMs and W-PAN FMs were peeled off the aluminum foil, cut into pieces, and placed into a chemical vapor deposition (CVD) furnace for heat treatment. The nanofiber mats were heated from room temperature to 230 °C in air at a rate of 5 °C min^{-1} and maintained at that temperature for 4 h for stabilization. The furnace was then heated to 800 °C at a rate of 5 °C min^{-1} under Ar flow (100 sccm) and maintained at this temperature for an additional 6 h for graphitization. Finally, the samples were cooled to room temperature under an Ar atmosphere. The synthesized products are denoted as W-*X*-CNFs, where *X* is the weight percent of tungsten to PAN powder in the W-PAN precursor.[29] Preoxidized W-PAN nanofiber mats were prepared as follows: the samples were heated from room temperature to 230 °C in air at a rate of 5 °C min^{-1}, maintained at this temperature for 4 h for stabilization, and then cooled to room temperature.

2.3. Characterizations. The morphology evolution of the prepared samples was observed by JSM-6700F field-emission scanning electron microscopy (FE-SEM; JEOL, Japan) at an acceleration voltage of 3 kV and by JSM-2100 transmission electron microscopy (TEM; JEOL, Japan) at an acceleration voltage of 200 kV. X-ray photoelectron spectra of the products were recorded using an X-ray photoelectron spectrometer (Kratos Aixs Ultra DLD) with an aluminum (mono) Kα source (1486.6 eV). The high-angle annual dark field scanning transmission electron microscopy (HAADF-STEM) images, STEM mappings, and line-scan energy-dispersive X-ray spectroscopy (EDX) images were recorded by a STEM (Tacnai G2 F30 S-Twin, Philips-FEI) at an acceleration voltage of 300 kV. The X-ray diffraction (XRD) patterns of the products were obtained on a diffractometer (Bruker AXS D8) using a Cu Kα radiation source (λ = 0.15418 nm) with a 2θ scan from 10° to 80° with a step size of 0.02.

2.4. Electrochemical measurements. The HER performance of the electrodes was measured in a 0.5 M H_2SO_4 electrolyte solution. The electrolyte was purged with nitrogen for at least 30 min before each test, and a nitrogen environment was maintained at all times to eliminate dissolved oxygen in the solution. Commercial Pt/C (Johnson-Matthey, 20 wt %) was cast on a glassy carbon disk of 3 mm diameter with a catalyst loading of 0.21 mg cm^{-2}. The samples were cut into 1 × 1 cm^{-2} squares and fixed with a Teflon electrode clamp to be used directly as the working electrode. A Pt mesh was used as the counter electrode, and a saturated calomel electrode (E (RHE) = E (SCE) + 0.265 V after calibration) was used as the reference electrode. All electrochemical measurements were performed on a CHI660E workstation (Shanghai Chenhua, Shanghai). Linear sweep voltammetry was conducted beginning at +0.3 V and ending at −0.5 V with a scan rate of 5 mV s^{-1}. The polarization curves were obtained after *iR*-compensation. Electrochemical impedance spectroscopy (EIS) was performed at a constant −0.25 V vs RHE while sweeping the frequency from 5 to 20 MHz with a 10 mV AC dither. The chronoamperometric response was obtained under a static overpotential of 0.215 V vs RHE. Current measurements were standardized through the catalyst's geometry and all potential values were plotted with reference to the reversible hydrogen electrode (RHE).

3. RESULTS AND DISCUSSION

According to the above discussions, we propose a facile method for the fabrication of WO_{3-x} on the surface of carbon nanofibers (Figure 1). First, W composites were homogeneously dispersed on PAN nanofibers by an electrospinning

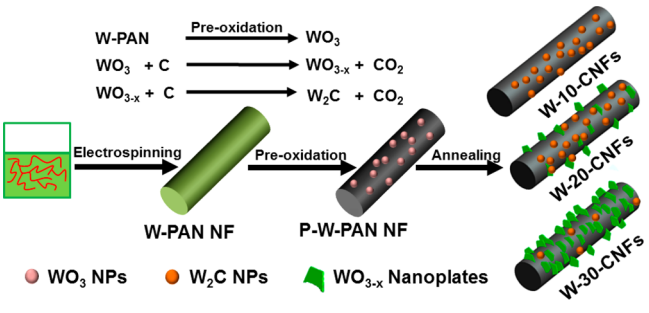

Figure 1. Schematic diagram of WO_{3-x} synthesis.

DOI: 10.1021/acsami.6b05245
ACS Appl. Mater. Interfaces XXXX, XXX, XXX−XXX

method. Then, after being preoxidized in air for 4 h, W composites became uniformly distributed on the surface of the nanofibers and reacted with oxygen, forming evenly distributed WO_3 nanoparticles (NPs). It was expected that additional W in the precursor would lead to more WO_3 NPs on the nanofiber surface. Carbon reduces WO_3 to W_2C on the surface when the temperature is increased to 800 °C because of its high activity.[22] However, the activity of carbon is relatively diminished with increasing amounts of WO_3, resulting in the formation of WO_{3-x} because of an inadequate reduction process.[23] Some WO_{3-x} nanoparticles possibly act as nucleation sites and attract neighboring nanoparticles to form clusters via van der Waals forces. In this case, the lateral growth of the clusters eventually forms a WO_{3-x} nanoplate on the surface of the CNFs.[30]

Figure S1a displays the TEM image of preoxidized W-PAN nanofibers with minute WO_3 nanoparticles uniformly distributed on their surface. In the XRD results of preoxide W-PAN nanofibers (Figure S1b), three strong peaks present at 26.3°, 33.6°, and 54.8° can be attributed to the (200), (220), and (420) planes, respectively, which are characteristic of cubic WO_3 (JCPDS card no. 46-1096). These results demonstrate that WO_3 is formed after the preoxidation treatment. Note that the broad peak at ~26.5° is indicative of the amorphous phase of PAN.

As shown in Figure 2, W_2C and WO_{3-x} were prepared on carbon nanofiber mats (CFMs) to different extents. The CFM

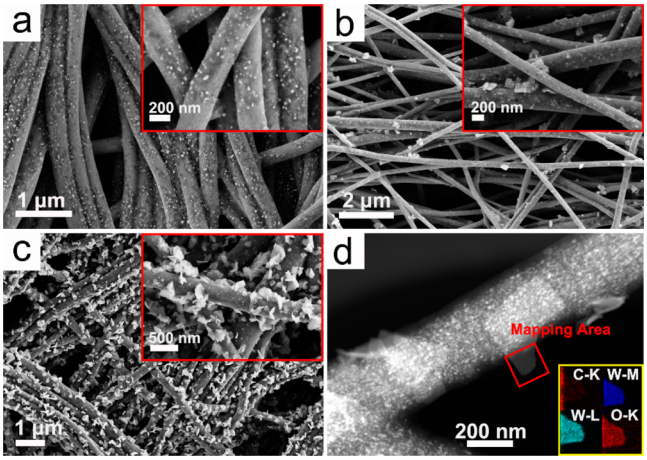

Figure 2. SEM images of (a) W-10-CNFs; (b) W-20-CNFs; (c) W-30-CNFs; (d) high-angle annular dark field (HAADF) STEM images of W-20-CNFs. Inset contains the elemental maps obtained from the mapping area in image d.

with a diameter of 200−300 nm is a three-dimensional substrate commonly employed in the electrocatalytic field. Figure 2a−c displays a distinct transition of the main morphology from nanoparticles of W_2C to nanoplates of WO_{3-x}. Figure 2b is a typical transitional period in which W_2C nanoparticles and WO_{3-x} nanoplates coexist. By comparing the nanoplates in parts b and c of Figure 2, it can be seen that the size of the WO_{3-x} nanoplates increases as the W content increases. In addition, the size of the nanoplates also markedly increases. WO_{3-x} nanoplates were evenly dispersed onto almost every carbon nanofiber in the present work. Thus, a high electrocatalytic performance for the HER was expected because of several WO_{3-x} active sites and the large specific surface area of the three-dimensional CFM.

A representative TEM image of a typical specimen (W-10-CNFs) is shown in Figure 3a. As seen, there are a large number

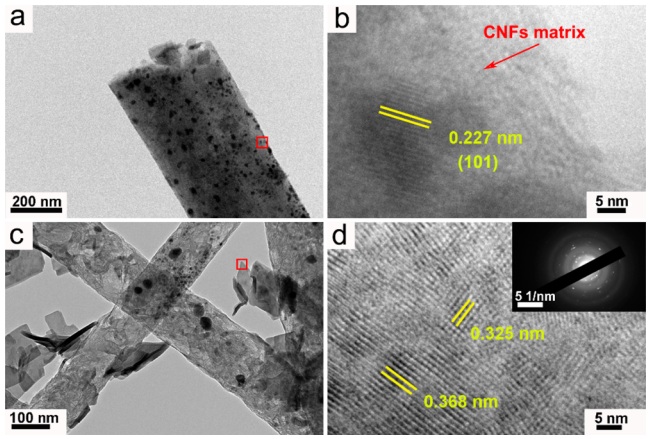

Figure 3. (a) Low-magnification TEM images of W-10-CNFs; (b) HRTEM image of the indicated rectangular area in image a; (c) low-magnification TEM images of W-20-CNFs; (d) HRTEM image of the indicated rectangular area in image c.

of W_2C nanoparticles evenly distributed on the CNF substrate. The corresponding high-resolution TEM (HRTEM) image of a W_2C nanoparticle shows that the lattice spacing is 0.277 nm, which can be ascribed to the (101) plane of hexagonal W_2C. A representative TEM image of another typical specimen (i.e., W-20-CNFs) exhibits that the as-prepared WO_{3-x} nanomaterials are rectangle-like nanoplates with edge lengths of 200−300 nm on the rough surface of the CNFs. Figure 3d displays the high-resolution TEM image of a representative single WO_{3-x} nanosheet from Figure 3c. As seen, the nanosheet is comprised of both amorphous and crystalline areas. The crystalline area has lattice spacings of 0.368 and 0.325 nm, which can be attributed to the peaks located at 24.1° and 27.4°, respectively, in the XRD pattern. The discontinuous crystalline area suggests poor crystallinity of the single nanoplate and suggests that several catalytically active sites could be exposed on the basal plane. In this regard, oxygen vacancies have been shown to act as active sites in TMOs for the HER.[6,31] For this reason, the additional oxygen vacancies in amorphous WO_{3-x} produce electrocatalytically active sites, which can enhance its performance for the HER. The crystalline area may benefit the electrochemical stability for the reaction, and the amorphous area is beneficial for the high electrocatalytic activity in acidic electrolytes. Spatially resolved W, C, and O elemental mapping obtained from the area in Figure 2b exhibits even distribution of W and O on the nanosheet, which suggests that the nanoplates consist of W and O (Figure 2d).

To further investigate the morphology of the W-20-CNFs, TEM and STEM analyses were conducted (Figure 4). Figure 4a shows a high-resolution TEM image of a carbon nanofiber with W-20-CNFs. As seen, there exist some nanoparticles with a lattice spacing of 0.266 nm, which can be ascribed to the spacing of the (101) plane of W_2C. The STEM-EDX mapping images of a single nanofiber confirm the existence and even distribution of W, C, and O. As shown in Figure 4d, the chemical composition was further confirmed by line-scan energy-dispersive X-ray (EDX) analysis on the backbone, which gives the relative intensities of the C, W, and O elements. As seen, the intensity of O is much lower than those of W and C, demonstrating that the nanoparticles distributed on the

DOI: 10.1021/acsami.6b05245
ACS Appl. Mater. Interfaces XXXX, XXX, XXX−XXX

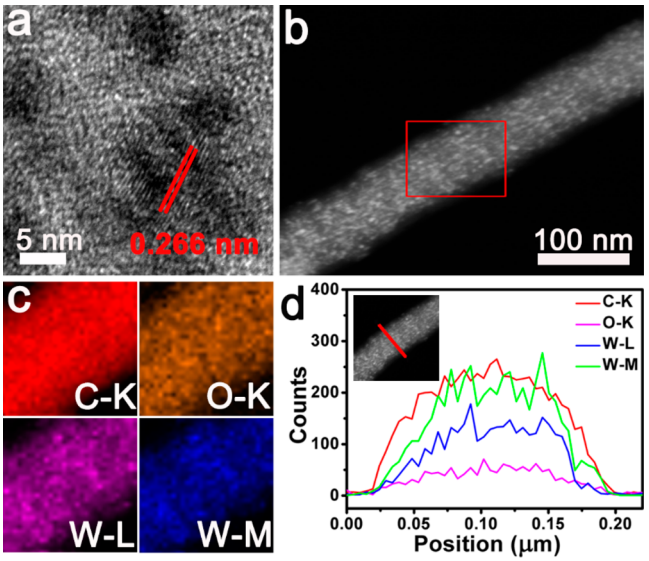

Figure 4. (a) HRTEM of W_2C nanoparticles on the W-20-CNFs; (b) HAADF-STEM image and (c) STEM-EDS (EDS = energy-dispersive spectroscopy) mapping images of the W-20-CNFs; (d) line scan EDX spectra of the W-20-CNFs.

nanofiber are W_2C and not WO_{3-x}. The TEM and STEM results of W-30-CNFs are shown in Figures S4 and S5; it can be seen that the nanoplates on the W-30-CNFs and W-20-CNFs have the same crystalline structure and composition. In addition, there are still some W_2C nanoparticles on the nanofibers of W-30-CNFs (Figure S5c), which are consistent with the XRD results (Figure 5f). To calculate the x value of the WO_{3-x} nanoplate, EDX analyses were conducted on the single nanoplates and the x values of W-20-CNFs and W-30-CNFs are determined as 1.64 and 1.53, respectively (Figure S4).

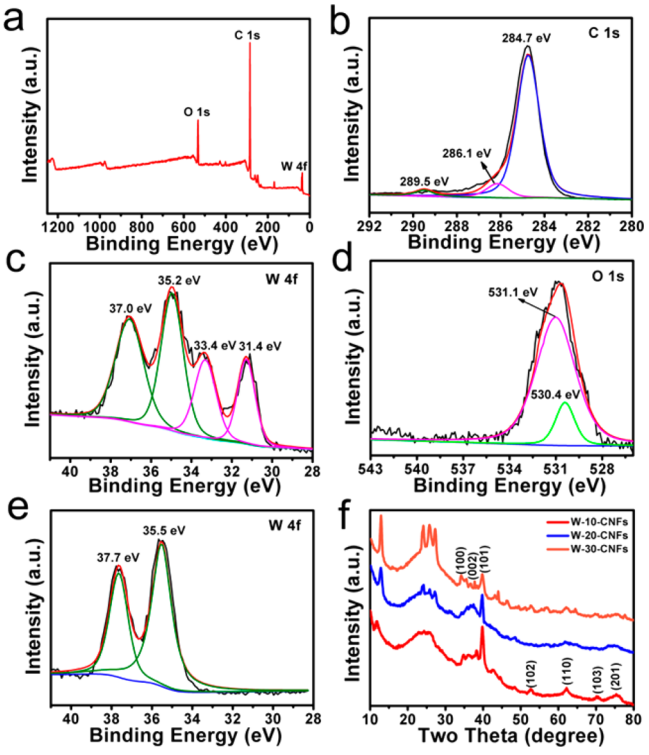

Figure 5. (a–d) XPS spectra of the collective, C 1s, W 4f, and O 1s of the W-20-CNFs, respectively; (e) XPS spectra of W 4f of the W-20-CNFs after preoxidation; (f) XRD patterns of the W-10-CNFs, W-20-CNFs, and W-30-CNFs.

To better illustrate the chemical states of O, C, and W on the surface of the resulting samples, XPS analyses of a typical sample (i.e., W-20-CNFs) were conducted. The weak peak at ~170 eV can be ascribed to the binding energy of S 2p. All the spectra were calibrated using the C 1s peak of carbon present at 284.50 eV. As shown in Figure 5c, there are two W states after deconvolution and each state is a pair of doublets. The peaks located at 35.2 (W $4f_{7/2}$) and 37.0 eV (W $4f_{5/2}$) correspond to the W−O bond of WO_{3-x}. Compared with the W 4f binding energy in WO_3, there is a red-shift in the binding energy of W, indicating that WO_3 has been partially reduced and that oxygen vacancies are present in WO_{3-x}.[6] In addition, oxygen vacancies in tungsten oxides were also evidenced by their strong vis/NIR absorption.[6,11] As can be seen in Figure S8, compared with W-10-CNFs, W-20-CNFs and W-30-CNFs show a big absorption tail in the range of 460−800 nm, strongly demonstrating the existence of a large amount of oxygen vacancies. Meanwhile, the energy bands at approximately 31.4 (W $4f_{7/2}$) and 33.4 eV (W $4f_{5/2}$) correspond to the W chemical state in the W−C bond, with good correspondence to the binding energy of W_2C.[32] For the O 1s spectra, the distinct peak at 531.1 eV is further separated into two peaks at 531.1 and 530.4 eV, which correspond to the C═O and W−O bonds, respectively.[33] Here, the C═O groups are attributed to the oxygen-containing groups on the surface of the carbon nanofibers.[33,34] The C 1s spectra show a distinct peak at 284.7 eV, corresponding to graphitized carbon.[34] The other two weaker peaks located at 286.1 and 289.5 eV are attributed to the W−C and C═O bonds, respectively.[33,34]

XRD analysis was performed to investigate the crystal structures of the three samples. The diffraction peaks of the W-10-CNFs are consistent with the standard pattern of hexagonal W_2C (JCPDS card no. 35-0776), indicating the high purity of the sample. The broad peaks at ~25.5° can be ascribed to the (002) plane of the graphite layers on the carbon nanofibers.[34] More importantly, the result confirms that the particles distributed on the surface of the W-10-CNFs are W_2C nanoparticles. Notably, one distinct peak at 13° and three distinct peaks located from 24.08° to 27.53° arise in the W-20-CNFs and W-30-CNFs, which correspond to the formation of WO_{3-x}.

In this work, the catalytic performances of the W-10-CNFs, W-20-CNFs, and W-30-CNFs were evaluated in a typical three-electrode electrochemical cell employing a 0.5 M H_2SO_4 electrolyte solution. Images of the cross sections were obtained because the catalysts were used directly as the working electrodes (Figure S2). The cyclic voltammetry experiments were recorded at 400 cycles to stabilize the samples and to eliminate surface contaminant.

As shown in Figure 6a, the CNFs exhibit negligible HER performance. In contrast, the W-30-CNFs catalysts show excellent HER activity with the low onset potential of 134 mV, with the current in the cathode rising rapidly under more negative potential. Moreover, in the entire potential area, overpotentials under the same current density of the W-30-CNFs are much lower than those of the CNFs, W-10-CNFs and W-20-CNFs. For instance, at a cathodic current density of 10 mA/cm^2, the overpotential of the W-30-CNFs sample is 185 mV, which is lower than that of the W-20-CNFs (227 mV) and

DOI: 10.1021/acsami.6b05245
ACS Appl. Mater. Interfaces XXXX, XXX, XXX−XXX

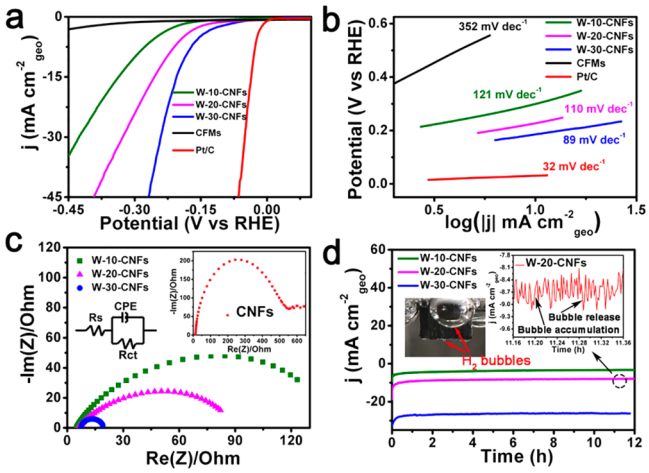

Figure 6. (a) Polarization curves obtained for the indicated electrodes; (b) corresponding Tafel plots; (c) electrochemical impedance spectra (EIS) of the indicated electrodes at η = 150 mV. Inset in image c: the equivalent circuit of the fitted curves. (d) Chronoamperometric response ($i - t$) under a static overpotential of −0.2 V vs RHE. Inset in panel d: digital photo of the H_2 bubbles formed on a W-20-CNFs membrane after 11 h. The enlargement of the area is denoted by the dashed circle.

W-10-CNFs (300 mV). To further investigation the HER performance of the catalysts, Tafel plots were fitted to the well-known Tafel equation ($\eta = a + b \log |j|$), in which j is the current density and b is the Tafel slope. It is understood that the latter quantity provides information on the fundamental steps in the HER; for this reason, values for the Tafel slope are given in Table 1. The first step of the reaction is the Volmer

Table 1. Electrocatalytic Performance of the Three Different Catalysts

	W-10-CNFs	W-20-CNFs	W-30-CNFs
η @ j = 10 mA cm^{-2} (mV)	300	227	185
Tafel slope (mV dec^{-1})	121	110	89
j_0 (mA cm^{-2})	0.122	0.186	0.239
C_{dl} (mF cm^{-2})	399	587	711

reaction, where hydronium ions are absorbed onto the active sites of the catalysts and gain electrons to generate absorbed hydrogen atoms. Subsequently, an electrochemical desorption step (Heyrovsky reaction) or recombination step (Tafel reaction) may occur. The commercial Pt/C catalyst gives a Tafel slope of 32 mV dec^{-1}, which is consistent with the reported results. The Tafel slope of the W-30-CNFs is 89 mV dec^{-1}, which is much lower than that of the W-10-CNFs (110 mV dec^{-1}) and W-20-CNFs (121 mV dec^{-1}), indicating that the catalyst operates via a Volmer−Heyrovsky mechanism in which electrochemical desorption is the rate-limiting step.[35] The relatively low Tafel slope for the W-30-CNFs is desirable to generate a large current density at smaller overpotential, which is beneficial in practical applications of catalysts for the HER. The electrospun CNFs can provide a large specific area to increase contact with the electrolyte and enhance the conductivity of the samples. The results of the HER performance of the W-20-CNFs and W-30-CNFs can be attributed to an appreciable difference in the amount of active sites. The W-10-CNFs display lower activity for the HER because they are mainly composed of W_2C nanoparticles uniformly dispersed on the CNF surface. Recent reports showed that the crystal phase fundamentally impacts the HER catalytic activity of transition metal carbide-based materials.[13] As shown in the XRD patterns, the crystal phase of W_2C is hexagonal, which may be the primary factor that influences HER activities.[1] Compared with WO_{3-x}, the W_2C hexagonal phase may exhibit relatively lower performance for the HER because of its intrinsic nature.[1,13] Hence, in the present investigations, the W content in the precursor has a significant influence on the HER performance by changing the composition and morphology of the catalysts on the CNFs. In addition, to exclude the influence of Pt particles' dissolution from counter electrode to the real HER performance of work electrode, we chose a typical sample (W-20-CNFs) to test the HER performance after 400 cyclic voltammetry scans using carbon electrode as the counter electrode. It can be seen that the two curves overlap well and the onset potential as well as current densities at any over potentials are comparable. (Figure S7). Therefore, the influence of Pt dissolution to the work electrode is negligible.

Exchange current density (j_0) is a vital measure of the HER performance of electrocatalysts by providing insight into their inherent activities. Typically, j_0 is deemed to be proportional to the active area on the catalyst's surface.[1,36] As shown in Table 1, the j_0 value calculated from the Tafel plot for the W-30-CNFs is 0.239 mA cm^{-2}, which is much higher than that for the W-10-CNFs (0.122 mA cm^{-2}) and W-20-CNFs (0.186 mA cm^{-2}). Further, the highest exchange current density for the W-30-CNFs is ascribed to both the high number of active sites on the WO_{3-x} nanoplates and the discontinuous crystallization on its basal plane. To estimate the effective surface area of the catalysts, one alternative method is to calculate the double layer capacitance (C_{dl}). To this end, CV plots were constructed under a potential range of 0.1−0.2 V vs RHE at scan rates of 0.5−5 mV s^{-1} without the presence of a faradic current (Figure S3). The C_{dl} values of the electrodes containing different samples were calculated and are listed in Table 1. The C_{dl} of the W-30-CNFs is 711 mF cm^{-2}, which is 1.78 and 1.21 times larger than the values for the W-10-CNFs (399 mF cm^{-2}) and W-20-CNFs (587 mF cm^{-2}), respectively. These data indicate that the W-30-CNFs possess a larger electrocatalytic effective surface area than the other two materials. The increase in the C_{dl} values demonstrates an increased number of active sites, which enhances the HER performance of the catalysts.

To investigate the kinetics of the electrode in the HER, electrochemical impedance spectroscopy (EIS) measurements were conducted. Figure 6c displays the Nyquist plots of various catalysts at η = 100 mV. No Warburg impedance is observed, indicating that the reaction is kinetically controlled. The emergence of only one semicircle in the plot indicates that the equivalent circuit is characterized by only one time constant.[5] Therefore, one simple equivalent electrical circuit for the HER can be used for its description. With respect to the solution resistance (R_s), the value for all electrodes is ∼3 Ω. It is worth noting that the charge transfer resistance (R_{ct}) among these catalysts is quite different. The value of R_{ct} for the W-30-CNFs electrodes is ∼15 Ω, which is conspicuously smaller than the values for the W-10-CNFs (ca. 170 Ω) and W-20-CNFs (ca. 85 Ω). As is well-known, R_{ct} is strongly associated with the kinetics of the HER, with a low R_{ct} value reflecting a higher electrocatalytic activity of the corresponding electrode.[37,38] Clearly, the W-30-CNFs possess an optimal electrocatalytic performance relative to the other electrodes. As discussed

DOI: 10.1021/acsami.6b05245
ACS Appl. Mater. Interfaces XXXX, XXX, XXX−XXX

above, WO_{3-x} possesses many oxygen vacancy defects that can enhance the conductivity of the catalyst and decrease the charge transfer resistance.[31] Therefore, by increasing the amount of WO_{3-x} in the catalysts, the corresponding R_{ct} values decrease, which is evident from a comparison of the R_{ct} values for the W-10-CNFs, W-20-CNFs, and W-30-CNFs materials.

Time-dependent current density at η = 280 mV in a 0.5 M H_2SO_4 electrolyte solution was measured to evaluate the stability of the electrode. The current density of the W-30-CNFs is ~26.5 mA cm^{-2}, which is 3.1 times larger than the current density of the W-20-CNFs (8.5 mA cm^{-2}) and 6.7 times larger than that of the W-10-CNFs (4.1 mA cm^{-2}). Degradation of the current density after 12 h is negligible for every catalyst. The alternate process of bubble accumulation and release can be observed as the characteristic serrated shape of the current (inset Figure 6d). Furthermore, the durability of a typical W-30-CNFs sample was examined. As shown in Figure 7b, the W-30-CNFs demonstrate a fairly stable activity within

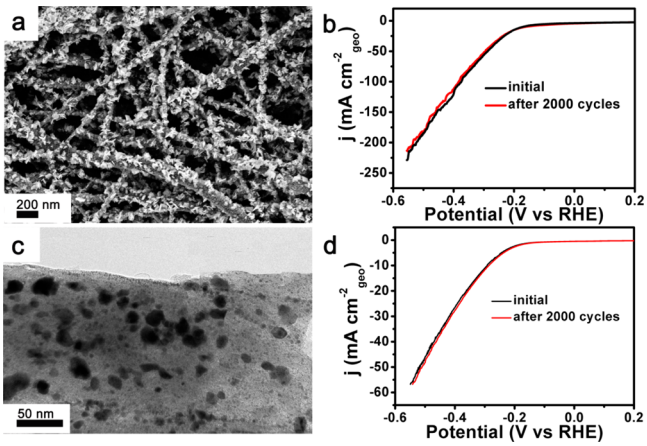

Figure 7. (a) SEM image of the W-30-CNFs catalyst after 2000 potential cycles; (b) polarization curves of the W-30-CNFs catalyst before and after 2000 potential cycles; (c) TEM image of the W-10-CNFs catalyst after 2000 potential cycles; (d) polarization curves of the W-10-CNFs catalyst before and after 2000 potential cycles.

the accelerated degradation measurement for 2000 cycles. To investigate the morphology of the sample following the stability tests, SEM images of the W-30-CNFs are shown in Figure 7a. As seen, the surface structure of WO_{3-x} remained identical to the original morphology without aggregation or detachment of the nanoplates, suggesting a favorable stability for the morphology of the electrode. Figure 7c is the TEM image of the W-10-CNFs, and there is no obvious aggregation or detachment of the W_2C nanoparticles. To investigate the change of the sample after stability test, digital photos are provided (Figure S6). It can be seen that the morphology of the catalytic material after 2000 recycles keeps well. As discussed above, WO_{3-x} was successfully fabricated via tuning the amount of tungsten chloride. With increasing tungsten chloride in the W-PAN precursor, WO_{3-x} was synthesized in the form of nanoplates, with consequent increases in the amount of WO_{3-x} as well. The superior HER activities of the WO_{3-x} nanoplates grown on CNFs are attributed to the following features: (1) Poor crystallinity of WO_{3-x} causes many defects in the lattice, leading to the exposure of more active sites. (2) WO_{3-x} possesses high electrical conductivity and thus promotes charge transfer in the HER.[12,29] (3) The large number of WO_{3-x} nanoplates densely distributed on the carbon nanofiber surface produces numerous electrochemically active sites. (4) The electrospun CNFs can provide a large specific area that increases the contact with the electrolyte solution and enhances the conductivity of the samples.

The W-10-CNFs electrodes display the lowest performance among the three electrodes examined. This result may be caused by the intrinsic nature of hexagonal W_2C, because different phases of W_2C have a significant influence on their associated electrochemical activities.[13,39] In addition, to the best of our knowledge, previously reported WO_2 or $WO_{2.72}$ nanostructures are mainly nanoparticles and nanotubes, which must be immobilized with a polymer binder on the electrode surface for electrochemical measurements.[40] However, in the present work, the catalysts on the CNFs can be directly employed as the electrode. Such an approach avoids loading on the carbon gassy electrode, which will be of great benefit for large-scale syntheses and practical applications.

4. CONCLUSIONS

Novel WO_{3-x} nanoplate electrochemical catalysts were fabricated on conductive carbon nanofiber mats without the use of toxic and dangerous reactant gases. The density of the WO_{3-x} nanoplates on the surface of carbon nanofibers can be easily tailored by adjusting the initial W content in the precursor. We find that the HER activities increase as the precursor W content increases. The synthesized WO_{3-x} has poor crystalline character that exposes numerous active sites. The catalysts were used directly as binder-free cathodes in the electrochemical measurements, and all of the catalysts display high current density, low overpotential, and long-term stability for splitting water. Notably, superior HER activities can be obtained by adjusting the amount of WO_{3-x} in the products. The remarkable electrocatalytic performances resulted from the poor crystallinity of WO_{3-x}, the high electrical conductivity of WO_{3-x}, and the use of electrospun CNFs. The present work provides a straightforward approach for synthesizing TMO-based carbon nanofiber mats that may have promising applications for the HER.

■ ASSOCIATED CONTENT

Supporting Information

The Supporting Information is available free of charge on the ACS Publications website at DOI: 10.1021/acsami.6b05245.

SEM, TEM, XRD, STEM, HRTEM, and EDX images; linear fitting of the capacitive currents of the catalysts vs scan rates; digital photo of W-30-CNFs before and after stability test; polarization curves with different counter electrodes; UV−vis diffuse reflectance spectra of the samples; table of XPS atomic concentrations of the samples (PDF)

■ AUTHOR INFORMATION

Corresponding Author

*Tel.: 86-571-86843763. Fax: 86-571-86843255. E-mail: du@zstu.edu.cn.

Notes

The authors declare no competing financial interest.

■ ACKNOWLEDGMENTS

This study was supported by the National Natural Science Foundation of China (NSFC) (Grant nos. 51373154 and

DOI: 10.1021/acsami.6b05245
ACS Appl. Mater. Interfaces XXXX, XXX, XXX−XXX

51573166), the Program for Innovative Research Team of Zhejiang Sci-Tech University, and the 521 Talent Project of Zhejiang Sci-Tech University.

REFERENCES

(1) Zhang, K.; Zhao, Y.; Fu, D.; Chen, Y. Molybdenum Carbide Nanocrystal Embedded N-doped Carbon Nanotubes as Electrocatalysts for Hydrogen Generation. *J. Mater. Chem. A* **2015**, *3*, 5783−5788.

(2) Walter, M. G.; Warren, E. L.; McKone, J. R.; Boettcher, S. W.; Mi, Q.; Santori, E. A.; Lewis, N. S. Solar Water Splitting Cells. *Chem. Rev.* **2010**, *110*, 6446−6473.

(3) Chang, Y. H.; Lin, C. T.; Chen, T. Y.; Hsu, C. L.; Lee, Y. H.; Zhang, W.; Wei, K. H.; Li, L. J. Highly Efficient Electrocatalytic Hydrogen Production by MoS_x Grown on Graphene-Protected 3D Ni Foams. *Adv. Mater.* **2013**, *25*, 756−760.

(4) Li, H. H.; Cui, C. H.; Zhao, S.; Yao, H. B.; Gao, M. R.; Fan, F. J.; Yu, S. H. Mixed-PtPd-Shell PtPdCu Nanoparticle Nanotubes Templated from Copper Nanowires as Efficient and Highly Durable Electrocatalysts. *Adv. Energy Mater.* **2012**, *2*, 1182−1187.

(5) Jin, Y.; Shen, P. K. Nanoflower-like Metallic Conductive MoO_2 as A High-performance Non-precious Metal Electrocatalyst for the Hydrogen Evolution Reaction. *J. Mater. Chem. A* **2015**, *3*, 20080−20085.

(6) Wu, R.; Zhang, J.; Shi, Y.; Liu, D.; Zhang, B. Metallic WO_2-Carbon Mesoporous Nanowires as Highly Efficient Electrocatalysts for Hydrogen Evolution Reaction. *J. Am. Chem. Soc.* **2015**, *137*, 6983−6986.

(7) Zheng, X.; Xu, J.; Yan, K.; Wang, H.; Wang, Z.; Yang, S. Space-confined Growth of MoS_2 Nanosheets within Graphite: The Layered Hybrid of MoS_2 and Graphene as An Active Catalyst for Hydrogen Evolution Reaction. *Chem. Mater.* **2014**, *26*, 2344−2353.

(8) Lin, C.-Y.; Mersch, D.; Jefferson, D. A.; Reisner, E. Cobalt Sulphide Microtube Array as Cathode in Photoelectrochemical Water Splitting with Photoanodes. *Chem. Sci.* **2014**, *5*, 4906−4913.

(9) Vrubel, H.; Hu, X. Molybdenum Boride and Carbide Catalyze Hydrogen Evolution in Both Acidic and Basic Solutions. *Angew. Chem.* **2012**, *124*, 12875−12878.

(10) Scanlon, M. D.; Bian, X.; Vrubel, H.; Amstutz, V.; Schenk, K.; Hu, X.; Liu, B.; Girault, H. H. Low-cost Industrially Available Molybdenum Boride and Carbide as "Platinum-like" Catalysts for the Hydrogen Evolution Reaction in Biphasic Liquid Systems. *Phys. Chem. Chem. Phys.* **2013**, *15*, 2847−2857.

(11) Tian, J.; Liu, Q.; Asiri, A. M.; Sun, X. Self-supported Nanoporous Cobalt Phosphide Nanowire Arrays: an Efficient 3D Hydrogen-evolving Cathode over the Wide Range of pH 0−14. *J. Am. Chem. Soc.* **2014**, *136*, 7587−7590.

(12) Fan, X.; Zhou, H.; Guo, X. WC Nanocrystals Grown on Vertically Aligned Carbon Nanotubes: An Efficient and Stable Electrocatalyst for Hydrogen Evolution Reaction. *ACS Nano* **2015**, *9*, 5125−5134.

(13) Wan, C.; Regmi, Y. N.; Leonard, B. M. Multiple Phases of Molybdenum Carbide as Electrocatalysts for the Hydrogen Evolution Reaction. *Angew. Chem.* **2014**, *126*, 6525−6528.

(14) Kong, D.; Wang, H.; Lu, Z.; Cui, Y. $CoSe_2$ Nanoparticles Grown on Carbon Fiber Paper: an Efficient and Stable Electrocatalyst for Hydrogen Evolution Reaction. *J. Am. Chem. Soc.* **2014**, *136*, 4897−4900.

(15) Liang, Y.; Li, Y.; Wang, H.; Zhou, J.; Wang, J.; Regier, T.; Dai, H. Co_3O_4 Nanocrystals on Graphene as A Synergistic Catalyst for Oxygen Reduction Reaction. *Nat. Mater.* **2011**, *10*, 780−786.

(16) Xi, G.; Ouyang, S.; Li, P.; Ye, J.; Ma, Q.; Su, N.; Bai, H.; Wang, C. Ultrathin $W_{18}O_{49}$ Nanowires with Diameters below 1 nm: Synthesis, Near-Infrared Absorption, Photoluminescence, and Photochemical Reduction of Carbon Dioxide. *Angew. Chem., Int. Ed.* **2012**, *51*, 2395−2399.

(17) Zhou, Y.; Hu, X. C.; Liu, X. H.; Wen, H. R. Core-shell Hierarchical WO_2/WO_3 Microspheres as An Electrocatalyst Support for Methanol Electrooxidation. *Chem. Commun.* **2015**, *51*, 15297−15299.

(18) Gulino, A.; Parker, S.; Jones, F. H.; Egdell, R. G. Influence of Metal-metal Bonds on Electron Spectra of MoO_2 and WO_2. *J. Chem. Soc., Faraday Trans.* **1996**, *92*, 2137−2141.

(19) Lukowski, M. A.; Daniel, A. S.; Meng, F.; Forticaux, A.; Li, L.; Jin, S. Enhanced Hydrogen Evolution Catalysis from Chemically Exfoliated Metallic MoS_2 Nanosheets. *J. Am. Chem. Soc.* **2013**, *135*, 10274−10277.

(20) Cheng, S.; Liu, H.; Logan, B. E. Power Densities using Different Cathode Catalysts (Pt and CoTMPP) and Polymer Binders (Nafion and PTFE) in Single Chamber Microbial Fuel Cells. *Environ. Sci. Technol.* **2006**, *40*, 364−369.

(21) Zhu, H.; Du, M.; Zhang, M.; Zou, M.; Yang, T.; Fu, Y.; Yao, J. The Design and Construction of 3D Rose-petal-shaped MoS_2 Hierarchical Nanostructures with Structure-sensitive Properties. *J. Mater. Chem. A* **2014**, *2*, 7680−7685.

(22) Liang, C.; Tian, F.; Li, Z.; Feng, Z.; Wei, Z.; Li, C. Preparation and Adsorption Properties for Thiophene of Nanostructured W_2C on Ultrahigh-surface-area Carbon Materials. *Chem. Mater.* **2003**, *15*, 4846−4853.

(23) Ledoux, M. J.; Hantzer, S.; Huu, C. P.; Guille, J.; Desaneaux, M.-P. New Synthesis and Uses of High-specific-surface SiC as A Catalytic Support That is Chemically Inert and Has High Thermal Resistance. *J. Catal.* **1988**, *114*, 176−185.

(24) Löfberg, A.; Frennet, A.; Leclercq, G.; Leclercq, L.; Giraudon, J. M. Mechanism of WO_3 Reduction and Carburization in CH_4/H_2 Mixtures Leading to Bulk Tungsten Carbide Powder Catalysts. *J. Catal.* **2000**, *189*, 170−183.

(25) Gruner, W.; Stolle, S.; Wetzig, K. Formation of CO_x Species during the Carbothermal Reduction of Oxides of Zr, Si, Ti, Cr, W, and Mo. *Int. J. Refract. Hard Met.* **2000**, *18*, 137−145.

(26) Alvarez-Merino, M. A.; Carrasco-Marín, F.; Fierro, J. L. G.; Moreno-Castilla, C. Tungsten Catalysts Supported on Activated Carbon: I. Preparation and Characterization after Their Heat Treatments in Inert Atmosphere. *J. Catal.* **2000**, *192*, 363−373.

(27) Ledoux, M. J.; Pham-Huu, C. Silicon Carbide: A Novel Catalyst Support for Heterogeneous Catalysis. *CATTECH* **2001**, *5*, 226−246.

(28) Zou, M.; Chen, J.; Xiao, L.; Zhu, H.; Yang, T.; Zhang, M.; Du, M. WSe_2 and $W(Se_xS_{1-x})_2$ Nanoflakes Grown on Carbon Nanofibers for the Electrocatalytic Hydrogen Evolution Reaction. *J. Mater. Chem. A* **2015**, *3*, 18090−18097.

(29) Taha, A. A.; Li, F. Porous WO_3−carbon Nanofibers: High-performance and Recyclable Visible Light Photocatalysis. *Catal. Sci. Technol.* **2014**, *4*, 3601−3605.

(30) Xiong, Y.; Xia, Y. Shape-Controlled Synthesis of Metal Nanostructures: The Case of Palladium. *Adv. Mater.* **2007**, *19*, 3385−3391.

(31) Lei, F.; Sun, Y.; Liu, K.; Gao, S.; Liang, L.; Pan, B.; Xie, Y. Oxygen Vacancies Confined in Ultrathin Indium Oxide Porous Sheets for Promoted Visible-light Water Splitting. *J. Am. Chem. Soc.* **2014**, *136*, 6826−6829.

(32) Aizawa, T.; Hishita, S.; Tanaka, T.; Otani, S. Surface Reconstruction of W_2C (0001). *J. Phys.: Condens. Matter* **2011**, *23*, 305007.

(33) Yang, T.; Du, M.; Zhu, H.; Zhang, M.; Zou, M. Immobilization of Pt Nanoparticles in Carbon Nanofibers: Bifunctional Catalyst for Hydrogen Evolution and Electrochemical Sensor. *Electrochim. Acta* **2015**, *167*, 48−54.

(34) Zhu, H.; Du, M.; Zhang, M.; Zou, M.; Yang, T.; Wang, L.; Yao, J.; Guo, B. Probing the Unexpected Behavior of AuNPs Migrating Through Nanofibers: A New Strategy for the Fabrication of Carbon Nanofiber−noble Metal Nanocrystal Hybrid Nanostructures. *J. Mater. Chem. A* **2014**, *2*, 11728−11741.

(35) Vilekar, S. A.; Fishtik, I.; Datta, R. Kinetics of the Hydrogen Electrode Reaction. *J. Electrochem. Soc.* **2010**, *157*, B1040−B1050.

(36) Chen, W. F.; Wang, C. H.; Sasaki, K.; Marinkovic, N.; Xu, W.; Muckerman, J. T.; Zhu, Y.; Adzic, R. R. Highly Active and Durable

DOI: 10.1021/acsami.6b05245
ACS Appl. Mater. Interfaces XXXX, XXX, XXX−XXX

Nanostructured Molybdenum Carbide Electrocatalysts for Hydrogen Production. *Energy Environ. Sci.* **2013**, *6*, 943−951.
(37) Krstajić, N.; Popović, M.; Grgur, B.; Vojnović, M.; Šepa, D. On the Kinetics of the Hydrogen Evolution Reaction on Nickel in Alkaline Solution: Part I. The Mechanism. *J. Electroanal. Chem.* **2001**, *512*, 16−26.
(38) Liu, S.; Yin, H.; Wang, H.; He, J. Electrochemical Performance of WO_2 Modified $LiFePO_4$/C Cathode Material for Lithium-ion Batteries. *J. Alloys Compd.* **2013**, *561*, 129−134.
(39) Liao, L.; Wang, S.; Xiao, J.; Bian, X.; Zhang, Y.; Scanlon, M. D.; Hu, X.; Tang, Y.; Liu, B.; Girault, H. H. A Nanoporous Molybdenum Carbide Nanowire as An Electrocatalyst for Hydrogen Evolution Reaction. *Energy Environ. Sci.* **2014**, *7*, 387−392.
(40) Manthiram, K.; Alivisatos, A. P. Tunable Localized Surface Plasmon Resonances in Tungsten Oxide Nanocrystals. *J. Am. Chem. Soc.* **2012**, *134*, 3995−3998.

DOI: 10.1021/acsami.6b05245
ACS Appl. Mater. Interfaces XXXX, XXX, XXX−XXX